Real-time imaging reveals the single steps of brain metastasis formation

Yvonne Kienast[1,2], Louisa von Baumgarten[1], Martin Fuhrmann[2], Wolfgang E F Klinkert[4], Roland Goldbrunner[3], Jochen Herms[2,5] & Frank Winkler[1,5]

Brain metastasis frequently occurs in individuals with cancer and is often fatal. We used multiphoton laser scanning microscopy to image the single steps of metastasis formation in real time. Thus, it was possible to track the fate of individual metastasizing cancer cells *in vivo* in relation to blood vessels deep in the mouse brain over minutes to months. The essential steps in this model were arrest at vascular branch points, early extravasation, persistent close contacts to microvessels and perivascular growth by vessel cooption (melanoma) or early angiogenesis (lung cancer). Inefficient steps differed between the tumor types. Long-term dormancy was only observed for single perivascular cancer cells, some of which moved continuously. Vascular endothelial growth factor-A (VEGF-A) inhibition induced long-term dormancy of lung cancer micrometastases by preventing angiogenic growth to macrometastases. The ability to image the establishment of brain metastases *in vivo* provides new insights into their evolution and response to therapies.

Metastasis formation is responsible for most cancer deaths[1]. Brain metastases, most often from lung and breast carcinomas and melanomas[1], induce a particularly high morbidity and mortality[2]. *In vivo* microscopy has been used to study cancer cell metastasis in various organs outside the brain[3–6]. However, individual cells can be followed for only short periods of time (for minutes up to a maximum of 24 h in the skin flap[7] and mammary fat pad[8]). Therefore, a full understanding of the essential and inefficient steps of the metastatic cascade[9], which would also have major implications for the design of improved therapies, has been difficult thus far. Many points, such as the mechanism of arrest[4,10] and the roles of extravasation[5], angiogenesis[9,11] and dormancy[12], remain controversial. Here we have established a new mouse model in which multiphoton laser-scanning microscopy (MPLSM)[13–16] is used to track the fate of metastasizing cancer cells in relation to blood vessels deep in the live brain.

RESULTS

In vivo imaging of brain metastasis formation
Real-time *in vivo* MPLSM through a chronic cranial window allowed the imaging of intra-arterially injected individual cancer cells expressing red fluorescent protein (RFP) in relation to perfused blood vessels (labeled by FITC-dextran) over minutes to months, up to a depth of 500 µm in the live brain of nude mice (**Fig. 1a**). RFP fluorescence intensity was stable over more than six passages *in vitro* and increased over time *in vivo* (in MDA-MB-435 cells by a factor of eight in 51 d (**Supplementary Fig. 1a**)). In the case of tumor cell regression, RFP fluorescence was maintained or increased before disappearance, which often had the morphological features of apoptosis (**Supplementary Fig. 1b**). No indirect (for example, vascular) signs of metastasis growth were seen *in vivo* over time in the absence of an RFP-expressing mass lesion (data not shown). We therefore conclude that no relevant loss of RFP expression occurred *in vivo*.

In the first days after hematogenous spread, a marked regression of cancer cells occurred (**Supplementary Fig. 2a**), which underscores the overall inefficiency of the late metastatic process[4]. Using *in vivo* MPLSM, we were able to identify four essential steps of successful macrometastasis formation in the brain: initial arrest at blood vessel branches, early extravasation, perpetuation of a perivascular position and angiogenesis or vessel cooption.

Initial arrest at blood vessel branches
In the first minutes after internal carotid artery injection, human PC14-PE6 lung carcinoma and MDA-MB-435 melanoma[17] cells moved passively with the blood flow in brain microvessels. Their speed was reduced within small microvessels with a diameter similar to that of the cell, especially at vascular branch points (**Fig. 1b–d**, **Supplementary Fig. 2b,c** and **Supplementary Video 1**).

We detected long-lasting cancer cell arrest (for a minimum of 60 s) in 9.8% of 61 PC14-PE6 lung carcinoma cells ($n = 4$ mice) and 7.7% of 39 MDA-MB-435 melanoma cells ($n = 3$ mice) analyzed. All of these arrested cells were stuck in vessel branches and showed a cell-vessel diameter ratio of 1. Cells left their initial resting position and reentered another resting position for up to 48 h (**Fig. 1e,f** and **Supplementary Video 2**).

Early extravasation
We observed metastasis growth only after successful extravasation (**Fig. 1g**) of single cancer cells. Of more than 100 cells analyzed in

[1]Department of Neurology, [2]Department of Neuropathology and [3]Department of Neurosurgery, Ludwig-Maximilians University, Munich, Germany. [4]Max Planck Institute of Neurobiology, Martinsried, Germany. [5]These authors contributed equally to this work. Correspondence should be addressed to F.W. (frank.winkler@med.uni-muenchen.de).
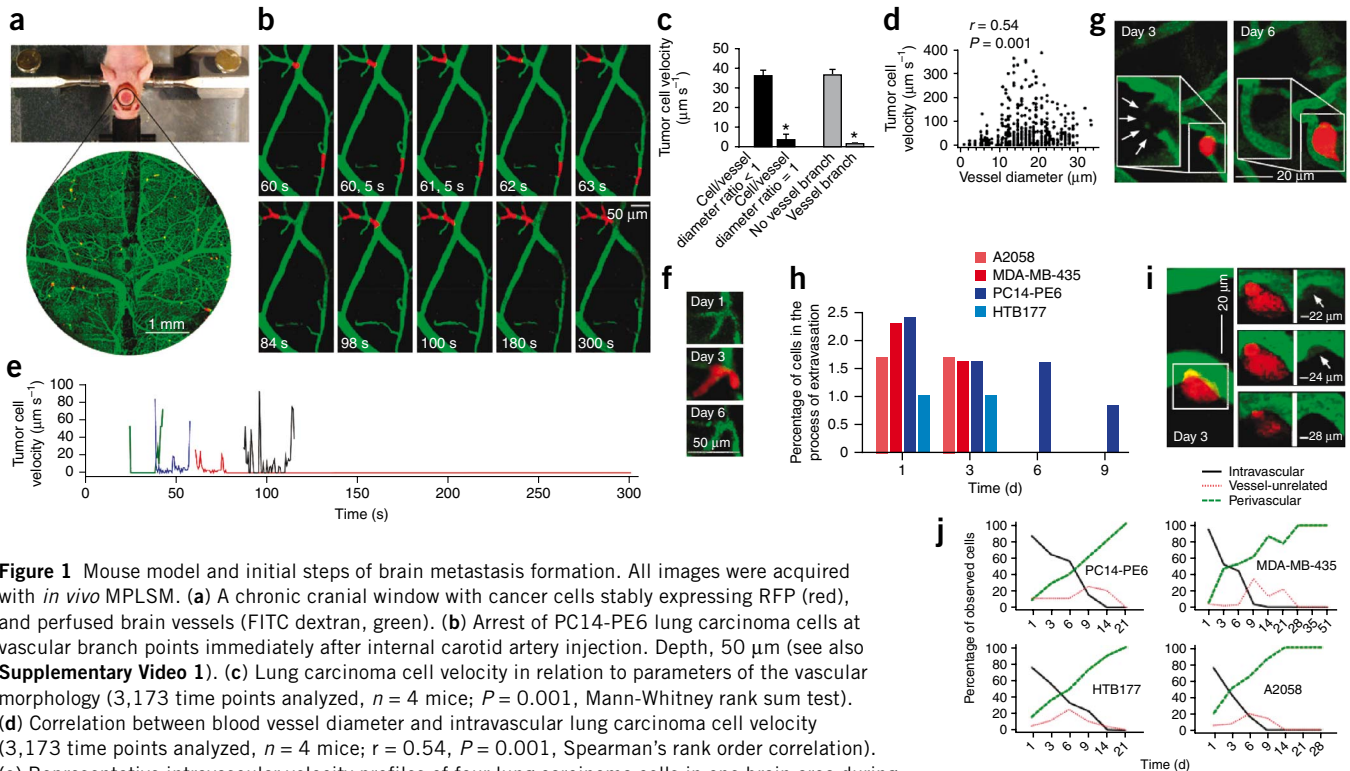
Figure 1 Mouse model and initial steps of brain metastasis formation. All images were acquired with *in vivo* MPLSM. (**a**) A chronic cranial window with cancer cells stably expressing RFP (red), and perfused brain vessels (FITC dextran, green). (**b**) Arrest of PC14-PE6 lung carcinoma cells at vascular branch points immediately after internal carotid artery injection. Depth, 50 μm (see also **Supplementary Video 1**). (**c**) Lung carcinoma cell velocity in relation to parameters of the vascular morphology (3,173 time points analyzed, *n* = 4 mice; *P* = 0.001, Mann-Whitney rank sum test). (**d**) Correlation between blood vessel diameter and intravascular lung carcinoma cell velocity (3,173 time points analyzed, *n* = 4 mice; r = 0.54, *P* = 0.001, Spearman's rank order correlation). (**e**) Representative intravascular velocity profiles of four lung carcinoma cells in one brain area during a 5-min period. (**f**) Transient lung carcinoma cell arrest at a vascular bifurcation at day 3 (depth, 120–160 μm). (**g**) An MDA-MB-435 melanoma cell located intravascularly (arrows; magnifications show the angiography only) escapes from the vascular system on day 6 (depth, 20–70 μm). (**h**) Proportion of lung carcinoma (PC14-PE6, HTB177) and melanoma (MDA-MB-435, A2058) cells in the process of extravasation over time. (**i**) An MDA-MB-435 melanoma cell caught in the process of extravasation. Arrows show cell-induced hole in the angiogram-only image. Depth of the large image, 20–30 μm). (**j**) Tumor cell location in relation to blood vessels over time. Cell and mouse numbers in **h** and **j** are provided in the Methods.

each of two melanoma (MDA-MB-435 and A2058) and two lung carcinoma (PC14-PE6 and HTB177) cell lines, extravasating cells could only be detected between day 1 and day 9 (**Fig. 1h**).

Cells caught in the process of extravasation showed intra- and extravascular parts with a narrowing at the position of the vascular wall (**Fig. 1i**). A time-lapse sequence of such A2058 cells revealed dynamic extensions and retractions of the extravascular protrusions (**Supplementary Video 3**). This suggests an active transmigration of metastasizing cancer cells through holes in the vascular wall. By day 14, all surviving cancer cells had extravasated into the surrounding tissue (**Fig. 1j**); the cancer cells that later successfully proliferated to macrometastases had left the blood vessel by day 3 (**Figs. 2** and **3**).

Perpetuation of a perivascular position
Extravasated cells lacking a close physical contact to the abluminal surface of the blood vessel wall regressed over time (**Fig. 1j** and **Fig. 2a**). All four investigated cancer cell lines were only successful in proliferation to micro- and macrometastases when a direct contact to the abluminal endothelial cell of a brain capillary was maintained over time in a pericyte-like position (**Fig. 1j** and **Fig. 2b,c**).

Furthermore, the two melanoma cell lines (MDA-MB-435, A2058) co-opted cerebral microvessels as leading structures for invasion and proliferation (**Fig. 2d–g** and **Supplementary Fig. 2d**). Along the way, they induced a characteristic remodeling leading to capillary loop formation[18] (**Fig. 2h**), but only at the site of direct cell-vessel contact (**Fig. 2i**). Capillary loop formation did not occur in lung carcinoma cells (PC14-PE6, HTB177) (**Fig. 3a**).

Angiogenesis or vessel cooption
Successful macrometastasis formation of PC14-PE6 lung carcinoma cells resulted from the proliferation of separate cell clusters in close proximity to each other (**Fig. 3a**). The simultaneous growth and subsequent fusion enabled the cluster to overcome a critical mean diameter (147 μm in PC14-PE6, 195 μm in HTB177), which always led to marked vascular changes (dilatation and tortuosity), shortly followed by angiogenesis that culminated in a period of fast and unrestrained growth (**Fig. 3a,b** and **Supplementary Fig. 2e,f**). Histological analysis of brain macrometastases from humans with this tumor type confirmed that marked angiogenesis and little infiltration of normal brain can also be found in humans (**Fig. 3c**).

In contrast, in mice melanoma macrometastases (>50 cells) originated from micrometastases (4–50 cells) with strong and reciprocal interactions with the preexisting microvasculature. Typically, solitary cells started to slowly proliferate along microvessels (**Fig. 2d–g** and **Fig. 3d**), inducing characteristic vascular loop formation of these vessels (**Fig. 2h,i** and **Fig. 3e**). More extensive vascular changes and occasionally angiogenesis occurred when large macrometastases had already formed, which took up to 51 d (average diameter: for MDA-MB-435, 382 μm; for A2058, 548 μm; **Fig. 3d,e** and **Supplementary Fig. 2e,f**). Vessel co-option in this type of brain metastasis can also be found in humans (**Fig. 3f**).

Unsuccessful micrometastasis proliferation
When extravasated PC14-PE6 lung carcinoma cells proliferated initially after extravasation (until day 9; **Fig. 3g**), they stopped and regressed in all foci where angiogenesis was not initiated (12 of 124 nodules in *n* = 6 mice).
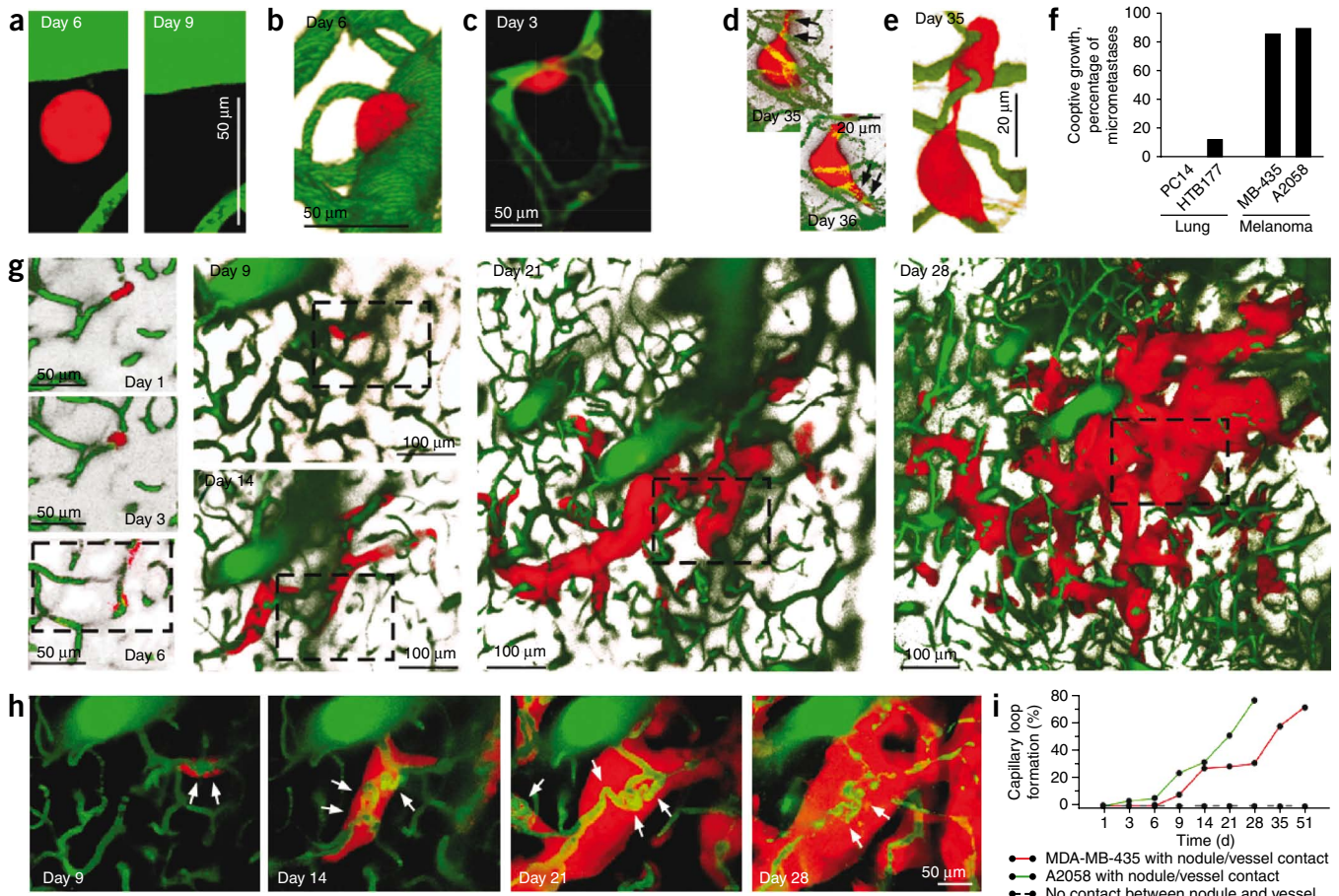
Figure 2 Interactions of cancer cells with the brain vasculature. (**a**) Regression of an extravasated PC14-PE6 lung carcinoma cell without close contact to a microvessel (depth, 10–30 μm). (**b**) A PC14-PE6 cell in a typical pericyte-like perivascular location (three-dimensional reconstruction; depth, 80–120 μm). (**c**) The abluminal surface of vascular endothelial cells (Tie2-GFP, green) has close physical contacts with an extravasated A2058 melanoma cell (depth, 10–20 μm). (**d**) Lamellipodium-like cellular protrusions (arrows), developed by invading perivascular MDA-MB-435 melanoma cells, stretch out along brain microvessels (depth, 80–150 μm). (**e**) MDA-MB-435 melanoma cells show longitudinal deformation while invading and proliferating along coopted brain microvessels, (three-dimensional reconstruction; depth, 120–450 μm). (**f**) Cooption of preexisting brain microvessels by growing and invading melanoma cells (MDA-MB-435, 12 of 14 nodules in four mice; A2058, seven of eight nodules in five mice), and in lung carcinoma (PC14-PE6, zero of 15 nodules in six mice; HTB177, one of 11 nodules in five mice). (**g**) Example for successful proliferation by vessel cooption of an A2058 melanoma cell. The box marks the same region over time (three-dimensional reconstruction; depth, 200–280 μm). (**h**) Vascular remodeling with capillary loop formation (arrows) at a site where A2058 melanoma cells have direct contact to the brain vasculature (depth, 200–210 μm). All images were acquired with *in vivo* MPLSM. (**i**) Quantification of capillary loop formation of cerebral microvessels with contact to MDA-MB-435 (*n* = 128) and A2058 (*n* = 107) melanoma cells and nearby vessels without this contact (*n* > 1,000 for each cell line) over time.

In mice given MDA-MB-435 melanoma cells (but not the lung carcinoma cell lines, **Supplementary Fig. 2g**), initially growing micrometastases that later regressed were located in regions of poor vascularization compared to those micrometastases that grew to macrometastases (**Fig. 3h,i**). This suggests that the absence of appropriate preexisting blood vessels for future co-option is fatal for this cell line. A2058 melanoma cells showed a similar trend (**Supplementary Fig. 2g**).

Dormancy
Tracking the fate of individual metastasizing cancer cells over many weeks revealed a small subset of vital cells that did not proliferate during the course of the experiment (**Fig. 4**). Of more than 100 cells analyzed, 4.0% (PC14-PE6; six cells in four mice), 3.1%; (MDA-MB-435; four cells in three mice) or 0% (HTB177, A2058) stayed dormant for up to 51 d (**Fig. 4c,d**). These long-term dormant cells were all solitary or in tiny clusters of up to three cells in strict perivascular localization.

Remarkably, all four dormant MDA-MB-435 melanoma cells showed a high motility in the brain, invading along preexisting blood vessels (**Fig. 4a**). Lung carcinoma cells also maintained a close association with brain vessels during dormancy, but we did not observe any motility (**Fig. 4b**); all five dormant PC14-PE6 cells were static (motile MDA-MB-435 versus static PC14-PE6 dormancy: *P* = 0.008, Fisher's exact test). Dormancy of larger cell clusters (micro- or macrometastases) did not occur.

The inefficient steps of brain metastasis
By tracking the fate of the two metastasizing lung cancer and two melanoma cell lines over many weeks, it was possible to determine the essential, efficient and inefficient steps (defined in the **Supplementary Methods**), as well as the dead ends, of the late metastatic cascade (**Fig. 4c,d**). For every cell or proliferating cell cluster, we could clearly determine the probability of further proliferation and reaching a next step, depending on its position and biological

Figure 3 Successful and unsuccessful macrometastasis formation. (**a**) Five foci of extravasated PC14-PE6 lung carcinoma cells in close proximity to each other on day 3 merge into one growing macrometastasis over time (depth: 50–450 μm). (**b**) Proliferation kinetics and vascular changes of successfully growing PC14-PE6 macrometastases (*n* = 3 macrometastases, three mice). (**c**) Representative brain metastasis of an individual who suffered from non–small-cell lung cancer. There is relatively clear demarcation of the macrometastasis (M, arrowheads) from the brain parenchyma (B) and a gross enlargement of some vessels within the tumor (V). (**d**) Macrometastasis formation by an MDA-MB-435 melanoma cell. There is slower growth along preexisting blood vessels. Depth, 50–350 μm. (**e**) Proliferation kinetics and vascular changes of successfully growing MDA-MB-435 macrometastases (*n* = 9 macrometastases, three mice). (**f**) Representative brain metastasis (arrowheads) of an individual with melanoma. Clusters of tumor cells (brown, melanin expression) are located along peritumoral blood vessels (arrows) in the surrounding brain parenchyma. The histological specimens in (**c**) and (**f**) were taken from routine brain biopsies (*n* = 5 per tumor type analyzed) and stained with H&E. (**g**) A PC14-PE6 lung carcinoma micrometastasis regresses on day 14. There are no vascular changes (depth, 0–100 μm). (**h**,**i**) Microvascular density in areas of regressing versus successfully growing MDA-MB-435 melanoma micrometastases (*n* = 7 metastases, *n* = 4 animals per group; *P* = 0.003, two-tailed *t* test). (**i**) Example for **h** (depth, 0–100 μm). Images in **a**,**d**,**g** and **i** were acquired with *in vivo* MPLSM.
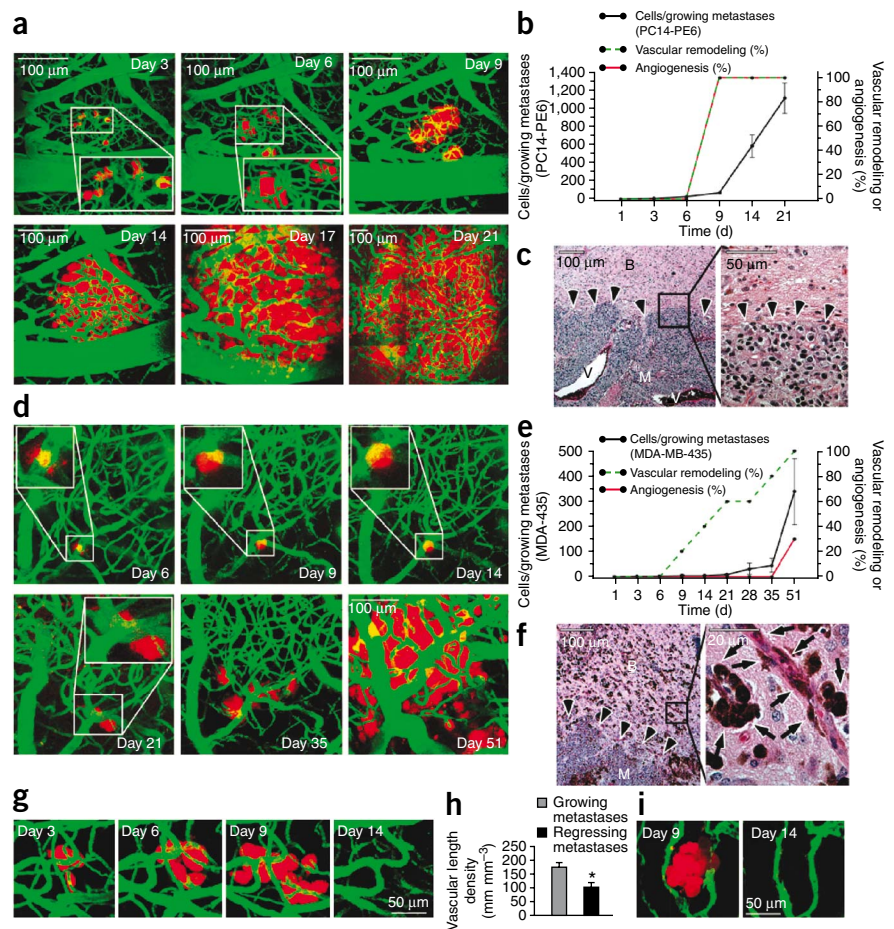
behavior. The inefficient steps were identical for both cell lines of one tumor type but differed between the tumor types; whereas lung carcinoma cells were most inefficient in proliferation from micro- to macrometastases (**Fig. 4c**), melanoma cells proliferated most inefficiently from perivascular single cells to micrometastases (**Fig. 4d**) (intravascular cell – perivascular cell, *P* < 0.001, Chi square; perivascular cell – micrometastasis, *P* = 0.003, Chi square; micrometastasis – macrometastasis, *P* < 0.001, Fisher's exact test).

The steps that never led to successful metastasis growth in both tumor types were perpetuation of an intravascular position, lack of close association with cerebral microvessels (vessel-unrelated cells), either directly after extravasation or after cessation of a primary perivascular position, and lack of vascular changes during metastasis growth. The four essential steps for successful metastasis formation have been demonstrated above and are summarized in **Figure 4e**.

VEGF-A inhibition induces dormancy of micrometastases

To confirm the relevance of cancer cell–blood vessel interactions for brain metastasis formation, we inhibited cancer cell–derived VEGF-A using bevacizumab. PC14-PE6 lung carcinoma cells constitutively expressed VEGF-A protein, but MDA-MB-435 melanoma cells did not (**Supplementary Fig. 3**).

When we started therapy 1 d after tumor cell injection, bevacizumab completely inhibited angiogenesis during lung carcinoma metastasis formation. This prevented micrometastases from thriving (**Fig. 5a**). Small micrometastases of fewer than or equal to nine cancer cells were kept in a state of chronic dormancy during

therapy. Furthermore, lung carcinoma cells started to proliferate intravascularly during VEGF-A inhibition (**Fig. 5b**) and switched to vessel co-option (**Fig. 5a**) and capillary loop formation (**Fig. 5c**), which we had observed before only in melanoma cells. The growth pattern of MDA-MB-435 melanoma cells was not influenced by VEGF-A inhibition (**Supplementary Fig. 4**). Quantification of the fate of metastases under long-term bevacizumab therapy confirmed that the therapeutic effect was due to (and essentially limited to) the induction of long-term dormancy by inhibiting angiogenesis (**Fig. 5d**,**e**).

DISCUSSION

In this study, we have established a new animal model for metastasis research. The model allows tracking of individual metastasizing cancer cells in an intact inner organ over months. This has been a major challenge of metastasis research during the past decades[2,19]. One-time histological experiments cannot track the future or the past of a phenomenon observed, and most *in vivo* imaging techniques have resolutions insufficient to study single cells[4]. Our model offers several advantages, as it is minimally invasive but sensitive to single cells; assesses the metastatic distribution throughout the cerebral cortex at all stages; differentiates between dormant, regressing and proliferating cells; and makes it possible to follow the growth of single cells into multicellular tumors over many weeks. In this way, we were able to detect previously hidden mechanisms of brain metastasis formation.

Using the new *in vivo* MPLSM mouse model, we found that the initial arrest of blood-borne cancer cells in the brain results from size
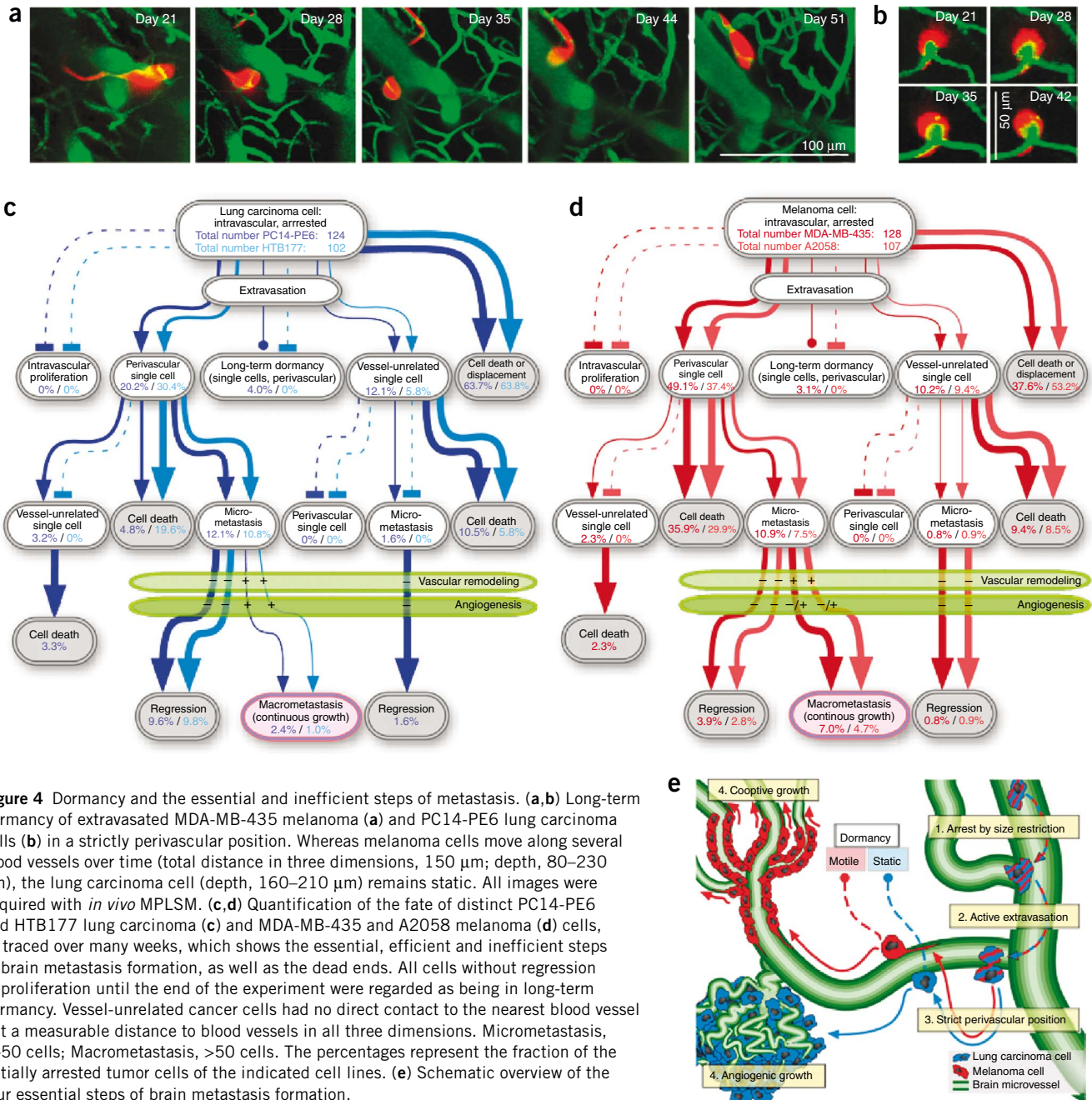
Figure 4 Dormancy and the essential and inefficient steps of metastasis. (**a,b**) Long-term dormancy of extravasated MDA-MB-435 melanoma (**a**) and PC14-PE6 lung carcinoma cells (**b**) in a strictly perivascular position. Whereas melanoma cells move along several blood vessels over time (total distance in three dimensions, 150 μm; depth, 80–230 μm), the lung carcinoma cell (depth, 160–210 μm) remains static. All images were acquired with *in vivo* MPLSM. (**c,d**) Quantification of the fate of distinct PC14-PE6 and HTB177 lung carcinoma (**c**) and MDA-MB-435 and A2058 melanoma (**d**) cells, as traced over many weeks, which shows the essential, efficient and inefficient steps of brain metastasis formation, as well as the dead ends. All cells without regression or proliferation until the end of the experiment were regarded as being in long-term dormancy. Vessel-unrelated cancer cells had no direct contact to the nearest blood vessel but a measurable distance to blood vessels in all three dimensions. Micrometastasis, 4–50 cells; Macrometastasis, >50 cells. The percentages represent the fraction of the initially arrested tumor cells of the indicated cell lines. (**e**) Schematic overview of the four essential steps of brain metastasis formation.

restriction and not vascular wall adhesion[20,21]. Furthermore, dynamic extravasation through small holes in the vascular wall[22] was essential for macrometastasis formation in the brain, which has been questioned before in the lung[5] and other organs[23,24]. Another essential step was the perpetuation of a strict perivascular position, which probably provides an optimal oxygen supply and access to nutrients[25,26] but might also increase the accessibility for therapeutics. The new mouse model can be used to further investigate these points.

Moreover, it is now possible to optimally detect cancer cell dormancy, a phenomenon of great clinical importance[1,12,19]. Single dormant cancer cells may find optimal survival conditions at their perivascular position. We also showed that anti–VEGF-A therapy, which has the potential to influence multiple steps of the metastatic cascade[27–30], can induce long-term dormancy of small, perivascular

lung carcinoma micrometastases[31]. This indicates an essential role of angiogenesis for lung metastasis growth early in the brain metastatic process.

Our model has some limitations, however. Long-term imaging was possible in only a proportion of the injected mice. Furthermore, because we injected a suspension of cultured cancer cells at one time point, we did not investigate the possible roles of concurrently metastasizing parenchyma cells[32] and the genetic and epigenetic diversity of the main tumor[33], including the impact of its preexistence.

The findings of our study can explain some of the clinical aspects of brain metastasis[34], including the highest propensity of melanomas to form brain metastases, the rapid development of brain metastases in individuals with lung carcinoma and the highest tendency of melanomas to produce multiple metastatic lesions (explained by

Figure 5 VEGF-A inhibition prevents early micrometastatic growth. (**a**) Therapy against VEGF-A with bevacizumab starting 1 d after lung cancer cell injection prevents the formation of new blood vessels. The small micrometastasis is rather kept in a state of chronic dormancy from day 28 on. Another bevacizumab-induced novelty of this tumor type is proliferation along preexisting brain microvessels (arrows; depth,100–170 μm). (**b**) Intravascular proliferation from day 3 on ends with the regression or displacement of the lung carcinoma cells on day 14 (depth, 60–100 μm). (**c**) Capillary loop formation occurs where lung carcinoma cells have contact to a brain microvessel during VEGF-A inhibition (depth, 240–300 μm). All images were acquired with *in vivo* MPLSM. (**d**) Proliferation kinetics of PC14-PE6 lung carcinoma metastases without signs of regression during bevacizumab treatment (start of therapy on day 1). n = 163 metastatic nodules in six mice. (**e**) Quantification of the metastatic fate of individual PC14-PE6 lung carcinoma nodules under bevacizumab versus control IgG treatment. Significant differences between the bevacizumab group and the IgG control group were limited to the last steps (macrometastasis formation versus chronic dormancy of micrometastases, P = 0.029, Fisher's exact test). The percentages represent the fraction of the initially arrested tumor cells of the indicated cell lines.
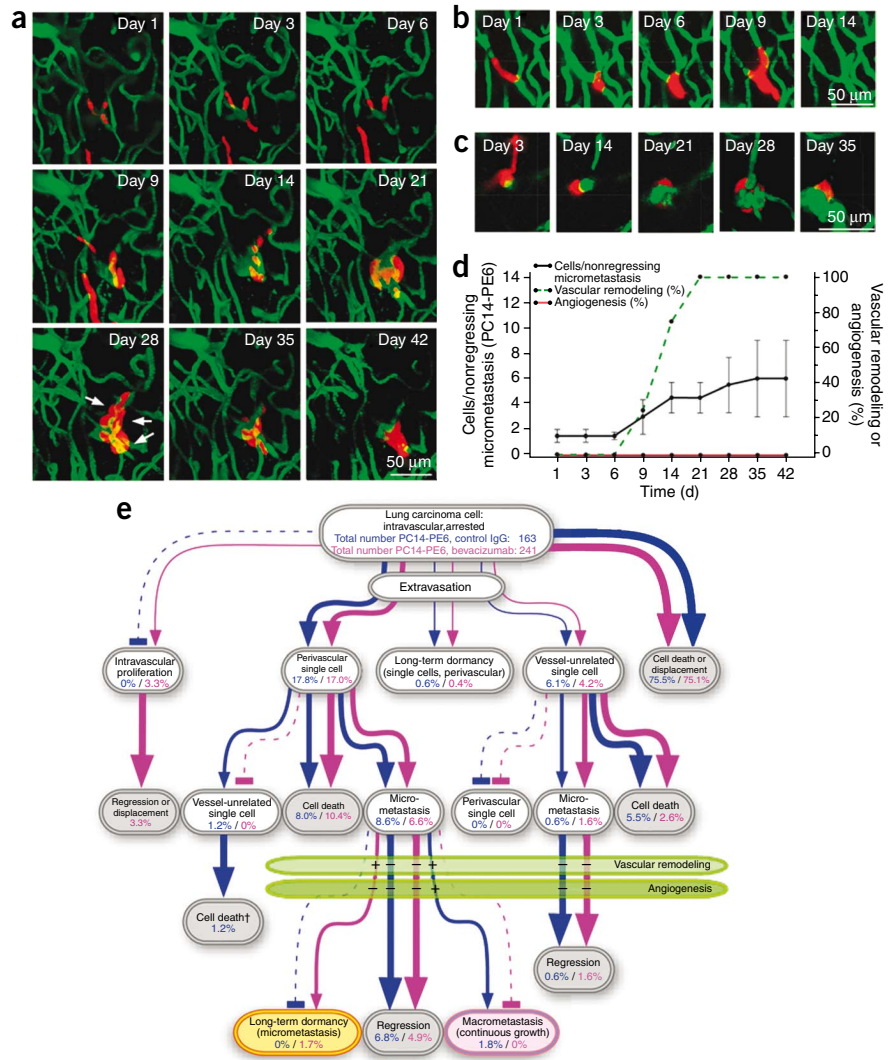
their clonal growth detected here and previously[35]). In the future, our new mouse model can be used to investigate the behavior of tumor cells that do not normally metastasize to the brain, which should help to gain further insight into the organ specificity of metastasis formation.

The ability to observe metastasis as a process rather than simply an end point has provided new insights into brain metastasis formation and an opportunity to experimentally address unanswered questions of metastasis research. This knowledge can be used to better tailor therapies in the future: the essential steps of the metastatic cascade should be the primary targets, the inefficient steps might be the easiest to inhibit[23] and the dead ends of metastasis formation can be ignored.

METHODS

Methods and any associated references are available in the online version of the paper at http://www.nature.com/naturemedicine/.

Note: Supplementary information is available on the Nature Medicine website.

AUTHOR CONTRIBUTIONS

Y.K. designed and performed experiments, carried out data analysis, prepared figures and wrote the manuscript. L.v.B. contributed to experimental work, especially to the generation of extravasation videos. M.F. provided technical support and methodological input regarding MPLSM. W.E.F.K. performed FACS sorting experiments. R.G. provided technical support and helpful discussions. J.H. contributed to the design of experiments and coordinated and supervised MPLSM. F.W. had the idea to establish the new animal model, designed and coordinated research, wrote the manuscript and supervised the project.

1. Steeg, P.S. Tumor metastasis: mechanistic insights and clinical challenges. *Nat. Med.* **12**, 895–904 (2006).
2. Palmieri, D., Chambers, A.F., Felding-Habermann, B., Huang, S. & Steeg, P.S. The biology of metastasis to a sanctuary site. *Clin. Cancer Res.* **13**, 1656–1662 (2007).
3. Wyckoff, J.B., Jones, J.G., Condeelis, J.S. & Segall, J.E. A critical step in metastasis: *in vivo* analysis of intravasation at the primary tumor. *Cancer Res.* **60**, 2504–2511 (2000).
4. Chambers, A.F., Groom, A.C. & MacDonald, I.C. Dissemination and growth of cancer cells in metastatic sites. *Nat. Rev. Cancer* **2**, 563–572 (2002).

5. Al-Mehdi, A.B. *et al.* Intravascular origin of metastasis from the proliferation of endothelium-attached tumor cells: a new model for metastasis. *Nat. Med.* **6**, 100–102 (2000).
6. Yamauchi, K. *et al.* Development of real-time subcellular dynamic multicolor imaging of cancer-cell trafficking in live mice with a variable-magnification whole-mouse imaging system. *Cancer Res.* **66**, 4208–4214 (2006).
7. Ito, S. *et al.* Real-time observation of micrometastasis formation in the living mouse liver using a green fluorescent protein gene-tagged rat tongue carcinoma cell line. *Int. J. Cancer* **93**, 212–217 (2001).
8. Kedrin, D. *et al.* Intravital imaging of metastatic behavior through a mammary imaging window. *Nat. Methods* **5**, 1019–1021 (2008).
9. Fidler, I.J., Yano, S., Zhang, R.D., Fujimaki, T. & Bucana, C.D. The seed and soil hypothesis: vascularisation and brain metastases. *Lancet Oncol.* **3**, 53–57 (2002).
10. Seitz, G. *et al.* Imaging of cell trafficking and metastases of paediatric rhabdomyosarcoma. *Cell Prolif.* **41**, 365–374 (2008).
11. Leenders, W.P. *et al.* Antiangiogenic therapy of cerebral melanoma metastases results in sustained tumor progression via vessel co-option. *Clin. Cancer Res.* **10**, 6222–6230 (2004).
12. Luzzi, K.J. *et al.* Multistep nature of metastatic inefficiency: dormancy of solitary cells after successful extravasation and limited survival of early micrometastases. *Am. J. Pathol.* **153**, 865–873 (1998).
13. Brown, E.B. *et al.* *In vivo* measurement of gene expression, angiogenesis and physiological function in tumors using multiphoton laser scanning microscopy. *Nat. Med.* **7**, 864–868 (2001).
14. Winkler, F. *et al.* Kinetics of vascular normalization by VEGFR2 blockade governs brain tumor response to radiation: role of oxygenation, angiopoietin-1 and matrix metalloproteinases. *Cancer Cell* **6**, 553–563 (2004).
15. Helmchen, F. & Denk, W. Deep tissue two-photon microscopy. *Nat. Methods* **2**, 932–940 (2005).
16. Hoffman, R.M. Advantages of multi-color fluorescent proteins for whole-body and *in vivo* cellular imaging. *J. Biomed. Opt.* **10**, 41202 (2005).
17. Rae, J.M., Creighton, C.J., Meck, J.M., Haddad, B.R. & Johnson, M.D. MDA-MB-435 cells are derived from M14 melanoma cells—a loss for breast cancer, but a boon for melanoma research. *Breast Cancer Res. Treat.* **104**, 13–19 (2007).
18. Döme, B., Timar, J. & Paku, S. A novel concept of glomeruloid body formation in experimental cerebral metastases. *J. Neuropathol. Exp. Neurol.* **62**, 655–661 (2003).
19. Townson, J.L. & Chambers, A.F. Dormancy of solitary metastatic cells. *Cell Cycle* **5**, 1744–1750 (2006).
20. Scherbarth, S. & Orr, F.W. Intravital videomicroscopic evidence for regulation of metastasis by the hepatic microvasculature: effects of interleukin-1α on metastasis and the location of B16F1 melanoma cell arrest. *Cancer Res.* **57**, 4105–4110 (1997).
21. Wood, S. Pathogenesis of metastasis formation observed *in vivo* in the rabbit ear chamber. *AMA Arch. Pathol.* **66**, 550–568 (1958).
22. Kawaguchi, T., Tobai, S. & Nakamura, K. Extravascular migration of tumor cells in the brain: an electron microscopic study. *Invasion Metastasis* **2**, 40–50 (1982).
23. Chambers, A.F., MacDonald, I.C., Schmidt, E.E., Morris, V.L. & Groom, A.C. Clinical targets for anti-metastasis therapy. *Adv. Cancer Res.* **79**, 91–121 (2000).
24. Koop, S. *et al.* Fate of melanoma cells entering the microcirculation: over 80% survive and extravasate. *Cancer Res.* **55**, 2520–2523 (1995).
25. Holash, J. *et al.* Vessel cooption, regression, and growth in tumors mediated by angiopoietins and VEGF. *Science* **284**, 1994–1998 (1999).
26. Calabrese, C. *et al.* A perivascular niche for brain tumor stem cells. *Cancer Cell* **11**, 69–82 (2007).
27. Yano, S. *et al.* Expression of vascular endothelial growth factor is necessary but not sufficient for production and growth of brain metastasis. *Cancer Res.* **60**, 4959–4967 (2000).
28. Küsters, B. *et al.* Vascular endothelial growth factor-A(165) induces progression of melanoma brain metastases without induction of sprouting angiogenesis. *Cancer Res.* **62**, 341–345 (2002).
29. Küsters, B. *et al.* Micronodular transformation as a novel mechanism of VEGF-A–induced metastasis. *Oncogene* **26**, 5808–5815 (2007).
30. Weis, S., Cui, J., Barnes, L. & Cheresh, D. Endothelial barrier disruption by VEGF-mediated Src activity potentiates tumor cell extravasation and metastasis. *J. Cell Biol.* **167**, 223–229 (2004).
31. Holmgren, L., O'Reilly, M.S. & Folkman, J. Dormancy of micrometastases: balanced proliferation and apoptosis in the presence of angiogenesis suppression. *Nat. Med.* **1**, 149–153 (1995).
32. Bouvet, M. *et al.* *In vivo* color-coded imaging of the interaction of colon cancer cells and splenocytes in the formation of liver metastases. *Cancer Res.* **66**, 11293–11297 (2006).
33. Ramaswamy, S., Ross, K.N., Lander, E.S. & Golub, T.R. A molecular signature of metastasis in primary solid tumors. *Nat. Genet.* **33**, 49–54 (2003).
34. Kaye, A.H. & Laws, E.R. *Brain Tumors: An Encyclopedic Approach.* Ch. 49, 999–1026 (Churchill Livingstone, London, 2001).
35. Fidler, I.J. & Talmadge, J.E. Evidence that intravenously derived murine pulmonary melanoma metastases can originate from the expansion of a single tumor cell. *Cancer Res.* **46**, 5167–5171 (1986).

ONLINE METHODS

Cell lines. We cultured A2058 human melanoma, MDA-MB-435 human melanoma[17] or melanoma-like[36] and HTB177 human lung cancer cell lines (American Type Culture Collection) and the PC14-PE6 human lung cancer cell line (kindly provided by I.J. Fidler) according to the vendor's specifications.

Red fluorescence protein gene transduction of cancer cells. We cloned the HindIII and NotI–flanked fragment from pDsRed2 (Clontech Laboratories), containing the full-length RFP cDNA, into pLNCX2 (Clontech Laboratories). We enriched RFP-transduced polyclonal sublines by FACS sorting (Vantage; Becton Dickinson).

Mouse experiments. We used nude mice (Charles River Laboratories) and crossed Tg(TIE2GFP)287Sato/J mice (which express GFP under the control of the endothelial lineage-specific Tie2 promoter; Jackson Laboratories) with nude mice to generate double-transgenic mice that combine immunodeficiency with stable GFP expression in endothelial cells. We prepared cranial windows (diameter 6 mm) as previously described[14]. For carotid artery injection, we conducted ligatures of the external and the common carotid artery[37] and injected 100 μl containing 1×10^5 cancer cells. In total, we successfully injected 15 mice with the cell line PC14-PE6-RFP, seven with HTB177-RFP cells, 14 with MDA-M-435-RFP and nine with A2058-RFP. Of these mice, 10 (PC14-PE6), five (HTB177), seven (MDA-MB-435) and five (A2058) could be used for *in vivo* multiphoton microscopy over time. To study the effects of VEGF-A inhibition, we injected mice intraperitoneally every other day with 15 mg per kg body weight bevacizumab or an IgG control antibody, starting on day 1 after injection (PC14-PE6, bevacizumab: four mice; IgG: six mice; MDA-MB-435: three mice per group). Mouse experiments were approved by the Administration of Upper Bavaria (#209.1/211-2531-94-05).

***In vivo* microscopy.** We used an upright laser scanning microscope (LSM 510 NLO, Zeiss) equipped with a MaiTai Titanium:Sapphire laser (710–920 nm, 10 W pump laser with automated dispersion; Newport Spectra Physics) for *in vivo* MPLSM. For fluorescence detection, we used two non-descanned detectors (Zeiss). A custom-made microscopy stage contained an integrated stereotactic mouse head holder (Narishige) to prevent breathing artifacts and to allow for repeated positioning. To visualize cerebral vessels, we injected 100 μl of a 10 mg ml^{-1} solution of FITC-labeled dextran (2M molecular weight, green) into the tail vein of the mouse. We acquired images at a wavelength of 750 nm on a region of 420×420 μm using a 20× Zeiss W Plan APOCHROMAT lens (numeric aperture 1.0). The image stack consisted of 250 single images from the brain surface (0 μm depth) to a depth of 500 μm, with a single image every 2 μm. We followed six cortical regions of interest, where tumor cells were visible, over time (days 1, 3, 6, 9 and 14 and then weekly). If tumor cells disappeared in one area, we imaged this area one last time, and then we selected another area of interest and followed it over time. Directly after cancer cell injection, we acquired images every 0.5 s in one focal plane (50 μm deep) for 5 min, followed by image stacks of 50 μm every 30 s for 1 h in a randomly selected area. We achieved retrieval of the same cells over time by using a coordinate-reading microscope, as well as using vascular pattern and unique branch points of the cortical vasculature as landmarks.

Quantifications. We observed and quantified a total of 128 individual metastasizing cells of the melanoma cell line MDA-MB-435 ($n = 4$ mice), 107 of the melanoma cell line A2058 ($n = 5$ mice), 124 of the lung carcinoma cell line PC14-PE6 ($n = 6$ mice) and 102 of the lung carcinoma cell line HTB177 ($n = 5$ mice) over up to 51 weeks. In addition, we imaged cancer cells for 30–60 min directly after intra-arterial injection (PC14-PE6: 61 cells, $n = 4$ mice; MDA-MB-435: 39 cells, 3 mice). To study the effects of VEGF inhibition, we analyzed 241 cells in four bevacizumab-treated mice and 163 cells in six IgG-treated mice. For detailed information on quantification of image parameters, see the **Supplementary Methods**.

Statistical analyses. Data are expressed as mean ± s.e.m. For comparison of groups, we used the two-tailed *t* test or the Mann-Whitney rank sum test. To test for correlations, we calculated the Spearman's rank correlation coefficient. To compare the frequencies of reaching a next step in the metastatic cascade, we used the Fisher's exact test or the Chi-square test. A level of $P < 0.05$ was regarded as statistically significant. We did all calculations with SigmaStat 3.5 software.

36. Sellappan, S *et al.* Lineage infidelity of MDA-MB-435 cells: expression of melanocyte proteins in a breast cancer cell line. *Cancer Res.* **64**, 3479–3485 (2004).
37. Schackert, G., Price, J.E., Bucana, C.D. & Fidler, I.J. Unique patterns of brain metastasis produced by different human carcinomas in athymic nude mice. *Int. J. Cancer* **44**, 892–897 (1989).